Atlantic waters inflow north of Svalbard: Insights from IAOOS observations and Mercator Ocean global operational system during N-ICE2015

Zoé Koenig, Christine Provost, Nicolas Villacieros Robineau, Nathalie Sennéchael, Amelie Meyer, Jean-Michel Lellouche, Gilles Garric

RESEARCH ARTICLE

Special Section:

Atmosphere-ice-ocean-ecosystem Processes in a Thinner Arctic Sea Ice Regime: The Norwegian Young Sea ICE Cruise 2015 (N-ICE2015)

Key Points:
- Operational 1/12° global ocean model remarkably reproduces observations in the complex region north of Svalbard
- Evidence of an important winter feature of AW inflow in the Arctic: the Yermak Pass Branch through the Yermak Plateau
- Modeled upwelling and convection contribute to realistic year-to-year variations in winter sea-ice edge location over the AW inflow

Correspondence to:
Z. Koenig,
zklod@locean-ipsl.upmc.fr

Atlantic waters inflow north of Svalbard: Insights from IAOOS observations and Mercator Ocean global operational system during N-ICE2015

Zoé Koenig[1] , Christine Provost[1] , Nicolas Villacieros-Robineau[1] , Nathalie Sennéchael[1] , Amelie Meyer[2] , Jean-Michel Lellouche[3] , and Gilles Garric[3]

[1]Laboratoire LOCEAN-IPSL, Sorbonne Universités (UPMC, Univ. Paris 6)-CNRS-IRD-MNHN, Paris, France, [2]Norwegian Polar Institute, Fram Centre, Tromsø, Norway, [3]Mercator Ocean, Research and Development, Ramonville Saint-Agne, France

Abstract As part of the N-ICE2015 campaign, IAOOS (Ice Atmosphere Ocean Observing System) platforms gathered intensive winter data at the entrance of Atlantic Water (AW) inflow to the Arctic Ocean north of Svalbard. These data are used to examine the performance of the 1/12° resolution Mercator Ocean global operational ice/ocean model in the marginal ice zone north of Svalbard. Modeled sea-ice extent, ocean heat fluxes, mixed layer depths and AW mass characteristics are in good agreement with observations. Model outputs are then used to put the observations in a larger spatial and temporal context. Model outputs show that AW pathways over and around the Yermak Plateau differ in winter from summer. In winter, the large AW volume transport of the West Spitsbergen Current (WSC) (∼4 Sv) proceeds to the North East through 3 branches: the Svalbard Branch (∼0.5 Sv) along the northern shelf break of Svalbard, the Yermak Branch (∼1.1 Sv) along the western slope of the Yermak Plateau and the Yermak Pass Branch (∼2.0 Sv) through a pass in the Yermak Plateau at 80.8°N. In summer, the AW transport in the WSC is smaller (∼2 Sv) and there is no transport through the Yermak Pass. Although only eddy-permitting in the area, the model suggests an important mesoscale activity throughout the AW flow. The large differences in ice extent between winters 2015 and 2016 follow very distinct atmospheric and oceanic conditions in the preceding summer and autumn seasons. Convection-induced upward heat fluxes maintained the area free of ice in winter 2016.

1. Introduction

The circulation and modification of the Atlantic Water (AW) inflow is a fundamental aspect of the Arctic Ocean. The AW inflow supplies heat and salt to the Arctic Ocean impacting the thermohaline structure of the water column and influencing the distribution of sea ice [e.g., *Rudels*, 2012]. The Atlantic Water enters the Arctic Ocean via two routes: through Fram Strait to the north of Svalbard and through the St. Anna Trough via the Barents Sea [e.g., *Dmitrenko et al.*, 2015]. Despite its importance to the Arctic system, the AW inflow (pathways and volume transports) north of Svalbard is still poorly known. The Arctic Ocean is a region where data are particularly sparse and model outputs are thus very useful to complement the analysis of in situ data. For instance, model outputs and in situ data have been combined to study the Arctic Circumpolar Boundary Current [*Aksenov et al.*, 2011] and to examine the seasonal cycle of AW temperature in the Arctic [*Lique and Steele*, 2012].

The area north of Svalbard is key to the Arctic Ocean heat budget as it is the major inflow point of AW (Figure 1). Two AW pathways have been identified: the shallow Svalbard Branch along the continental slope of Svalbard, and the deeper Yermak Branch on the western side of the Yermak Plateau [*Cokelet et al.*, 2008]. The shallow Svalbard Branch generates large sea ice melt along the continental slope, and leaves this area called the Whalers Bay free of ice in winter [e.g., *Ivanov et al.*, 2012; *Onarheim et al.*, 2014].

The Norwegian young sea ICE (N-ICE2015) campaign [*Granskog et al*, 2016; *Meyer et al.*, 2017] took place from January until June 2015 north of Svalbard to study the Arctic atmosphere, ice, ocean, and biology. IAOOS (Ice Atmosphere Ocean Observing System) platforms carrying ice mass balance instruments and ice-tethered ocean profilers provided new insights on oceanic conditions in winter north of Svalbard (C. Provost et al., Observations of snow-ice formation in a thinner Arctic sea ice regime during the N-ICE2015 campaign:
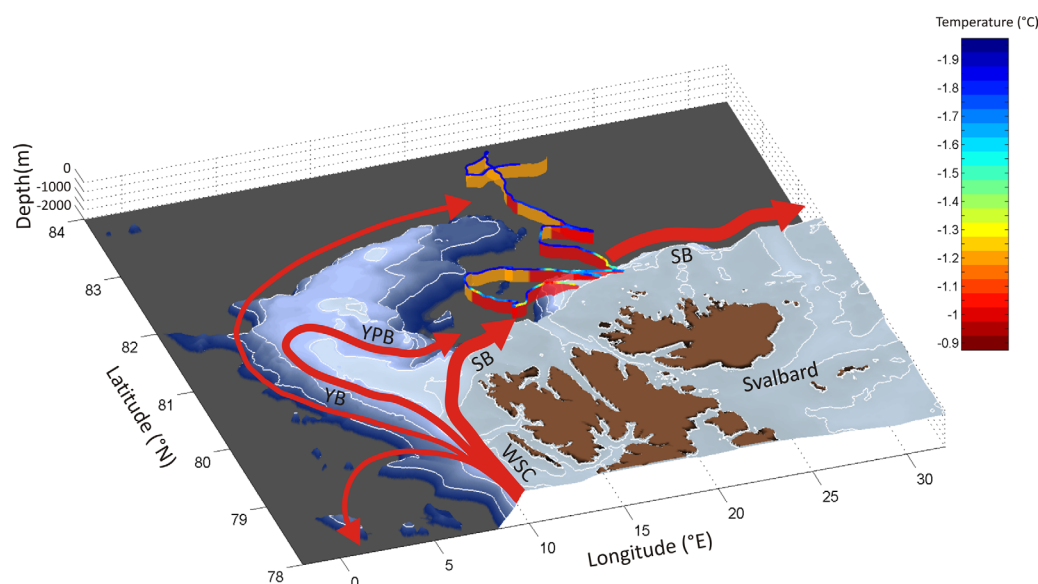
Figure 1. Summary of the in situ data results from *Koenig et al.* [2016] and *Provost et al.* [submitted]. The background of the 3-D plot is the bathymetry from IBCAO (http://www.ngdc.noaa.gov/mgg/bathymetry/arctic/arctic.html). The red lines are the warm water paths. YB: Svalbard Branch. WSC: West Spitsbergen Current. YPB: Yermak Pass Branch. SB: Svalbard Branch. Summary of the warm water layer is the orange/red ruban: orange corresponds to Modified Atlantic Water and red to Atlantic Water. The overlaying data are the surface temperature obtained from the SIMBA instrument (colorbar on the side).

Influence of basal ice melt and storms, submitted to *Journal of Geophysical Research Oceans*, 2017) [*Koenig et al.*, 2016] (Figure 1). The parts of the Nansen Basin and of the Svalbard northern continental slope crossed during the platform drift featured distinct hydrographic properties and ice-ocean exchanges. In the Nansen Basin, the quiescent warm layer was capped by a stepped halocline (60 and 110 m) and a deep thermocline (110 m). Ice was forming and the winter mixed layer salinity was larger by $\sim$0.1 g.kg^{-1} than previously observed [*Koenig et al.*, 2016]. Over the Svalbard continental slope, AW was very shallow (20 m from the surface) and extended offshore from the 500 m isobath by a distance of about 70 km. Considerable basal sea-ice melt was observed with ocean-to-ice heat fluxes inferred from ice mass balance instruments peaking to values of 400 Wm^{-2} (C. Provost et al., submitted manuscript, 2017).

Operational models, such as the one from Mercator Ocean, use a global network of satellite and ocean-based measuring systems to monitor and forecast the world's oceans [*Lellouche et al.*, 2013]. Operational models assimilate ocean measurements and use them to produce estimates of the full depth ocean state including sea-ice. Then, forced at the surface by weather prediction systems, these models forecast ocean currents, temperature, salinity, sea-ice and biogeochemistry. Quality control of operational ocean forecast system is a core activity in operational centers and independent data, not assimilated in the operational model, are used to evaluate model performances [e.g., *Hernandez et al.*, 2015; *Ryan et al.*, 2015]. AW inflow is well represented in operational model outputs as the models assimilate, among other observations, data in Fram Strait [*Lien et al.*, 2016]. In contrast, free-running models do not reproduce well the AW inflow and show large differences in the AW propagation through the Arctic Ocean [*Ilicak et al.*, 2016]. The low horizontal resolution of these free-running models (larger or equal to 0.25°) can partially explain the difficulties in representing the AW inflow and propagation. Indeed, the deformation radius in the Arctic Ocean is small, less than 10 km [*Zhao et al.*, 2014; *Nurser and Bacon*, 2013].

We took advantage of the observations gathered by IAOOS platforms during the N-ICE2015 campaign to evaluate 1/12° Mercator Ocean operational model north of Svalbard in winter (Figure 1). The IAOOS platform provided the first hydrographic data in the region in winter. Numerous processes at play in the Marginal Ice Zone (MIZ) north of Svalbard make comparisons between model outputs and observations a stringent test for the model performance, especially as the Mercator Ocean model does not explicitly represent some processes such as tides and inertial waves. Note that the model 1/12° horizontal resolution grid,

4–5 km resolution north of Svalbard, is only an eddy-permitting grid in the area as the Rossby deformation radius is about 6–8 km [*Zhao et al.*, 2014; *Nurser and Bacon*, 2013].

The main goal of the present study is to provide answers to the two following questions: (1) How does Mercator Ocean global operational model perform in the winter north of Svalbard? (2) What can we learn about the spatial and temporal context of N-ICE2015 IAOOS data from model outputs? We used outputs from the Mercator Ocean model from January 2014 to March 2016 to put in situ Lagrangian observations of midwinter 2015 in a larger spatial and temporal context. In particular, we focus on AW circulation (pathways, volume transports, heat contents) and surface conditions (ice edge location and upper ocean temperatures).

Mercator Ocean global operational model outputs and IAOOS data are introduced in section 2. Model outputs are compared to the extensive winter observational data set in section 3. Once the model outputs are evaluated, they are used to discuss AW inflow and seasonal and year-to-year variations in section 4, and upper ocean temperature and ice edge location in section 5. Finally, section 6 summarizes the results and puts forward perspectives.

2. Description of Operational System and In Situ Data

2.1. Mercator Ocean Operational System and First Assessment

Hindcasts from the global $1/12°$ real-time operational system developed at Mercator Ocean for the Copernicus Marine Environment Monitoring Service (CMEMS; http://marine.copernicus.eu/) are used. The system is based on the NEMO (Nucleus for European Modelling of the Ocean) [*Madec*, 2008] platform and uses a multidata and multivariate reduced order Kalman filter based on the Singular Extended Evolutive Kalman (SEEK) filter formulation introduced by *Pham et al.* [1998]. The model has 50 vertical levels with typically 1 m resolution at the surface decreasing to 450 m at the bottom and 22 levels within the upper 100 m. The model uses the LIM2 thermodynamic-dynamic sea ice model and is driven at the surface by atmospheric analysis and forecasts from the IFS (Integrated Forecasting System) operational system at ECMWF (European Centre for Medium-Range Weather Forecasts). The assimilated observations are along-track satellite altimetry, sea surface temperature (SST), and in situ vertical profiles of temperature and salinity. The data assimilation scheme is fully operational for SST warmer than $-1°C$ and is switched off for SST colder than the freezing point (in ice covered areas). Sea ice is not assimilated in this version of the model. Full description of the system components is available in *Lellouche et al.* [2013]. The model outputs have a daily resolution and are used from 8 January 2014 to 15 March 2016 over a region extending from -5 to $35°E$ in longitude and from 78 to $84°N$ in latitude.

A preliminary comparison of model outputs with data from the mooring transect monitoring the flow at Fram Strait (79°N across the West Spitzbergen Current) since 1997 [*Beszczynska-Moller et al.*, 2012] shows that the model produces reasonable seasonal cycles in volume transports and temperatures at that location. Indeed, the model provides a northward AW (with T>2°C) volume transport of 3.7 ± 1.4 Sv in winter and 1.7 ± 1.5 Sv in summer in 2015, in agreement with the 13 year statistics (1997–2010) from in situ data [*Beszczynska-Moller et al.*, 2012]. The monitoring array showed that the northward volume transport of AW (T> 2°C) at 79°N undergoes a marked seasonal cycle with a maximum in winter (4 ± 1 Sv) and a minimum in summer (2 ± 1 Sv) [*Beszczynska-Moller et al.*, 2012]. Model temperature in Fram Strait are also in agreement with the mooring transect at 79°N (4.5°C at the surface and 3°C at 500 m, to be compared with Figure 2 in *Beszczynska-Moller et al.* [2012]).

Further East, at 30°E and 81.8°N, the model temperature outputs can be compared with mooring data [*Ivanov et al.*, 2009] and to temperature from the A-TWAIN campaign [*Våge et al.*, 2016]. Seasonal variations in the model temperature outputs are in good agreement with NABOS (Nansen and Amundsen Basins Observational System, http://nabos.iarc.uaf.edu/) data ($\sim 2.7 \pm 0.3°C$ in summer and $\sim 3.5 \pm 0.4°C$ in winter). The large temperatures observed recently at 30°E are in the variability range of the modeled temperature at that location [*Våge et al.*, 2016].

Comparisons to contemporaneous data can be made with satellite data. Sea-ice concentration maps from the model compare rather well with maps derived from AMSR-2 (Advanced Microwave Scanning Radiometer) brightness temperature data with a 6 km × 6 km spatial resolution (retrieved from https://www.zmaw.de/)
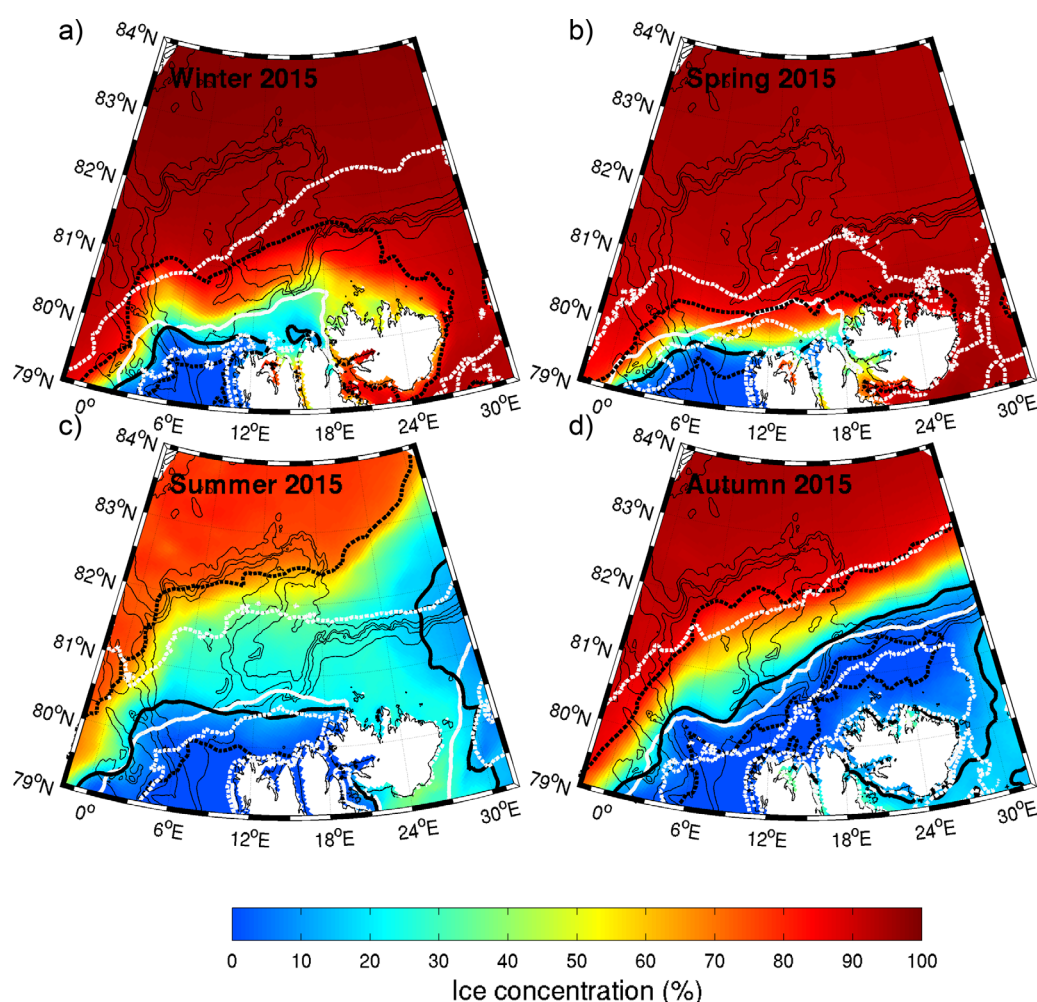
Figure 2. Seasonal comparisons of model output sea ice cover (in %) with AMSR-2 data. (a) Mean for January–February–March (Winter), (b) Mean for April–May–June (Spring), (c) Mean for July–August–September (Summer), and (d) Mean for October–November–December (Autumn). The colored background is the ice cover from the model outputs. The thick white (black) solid line is the mean ice edge from AMSR-2 data (model outputs), 15% ice cover averaged over the same periods. The dashed white (black) lines are the northern/southern location of the ice edge from AMSR-2 data (model outputs) over the same period. Thin black lines are bathymetric contours.

(Figure 2). The 15% contour line is considered as the ice edge. Winter, spring, summer, and autumn 2015 sea-ice edges from model outputs are in good agreement with the satellite-derived ice edge with zonal differences of less than 0.5° (Figure 2).

These preliminary comparisons are rather encouraging and we proceed to more detailed comparisons with the winter ocean and sea-ice IAOOS data presented below.

2.2. Data: IAOOS Ocean and Ice Data Acquired During N-ICE2015

Two IAOOS platforms were deployed in January 2015 during N-ICE2015 experiment less than 500 m apart. They were equipped with a SIMBA instrument (SAMS Ice Mass Balance for the Arctic) [*Jackson et al.*, 2013; *Provost et al.*, 2015] and an ice-tethered ocean profiler [*Koenig et al.*, 2016]. A tent-covered testing-hole with an ice-tethered profiler was also deployed less than 500 m apart from the two IAOOS platforms. Five other SIMBAs were deployed in a 20 km radius from the IAOOS platforms (C. Provost et al., submitted manuscript, 2017).

SIMBA repeatedly observed temperature and thermal resistivity proxy profiles with 2 cm vertical resolution in air, snow, ice, and ocean below. The 7 SIMBAs located in a 20 km radius from the IAOOS platform are averaged. Drift speed, snow depth, ice thickness, near surface ocean temperature and ocean heat flux were derived from the SIMBA observations (Figure 3) (C. Provost et al., submitted manuscript, 2017). We first
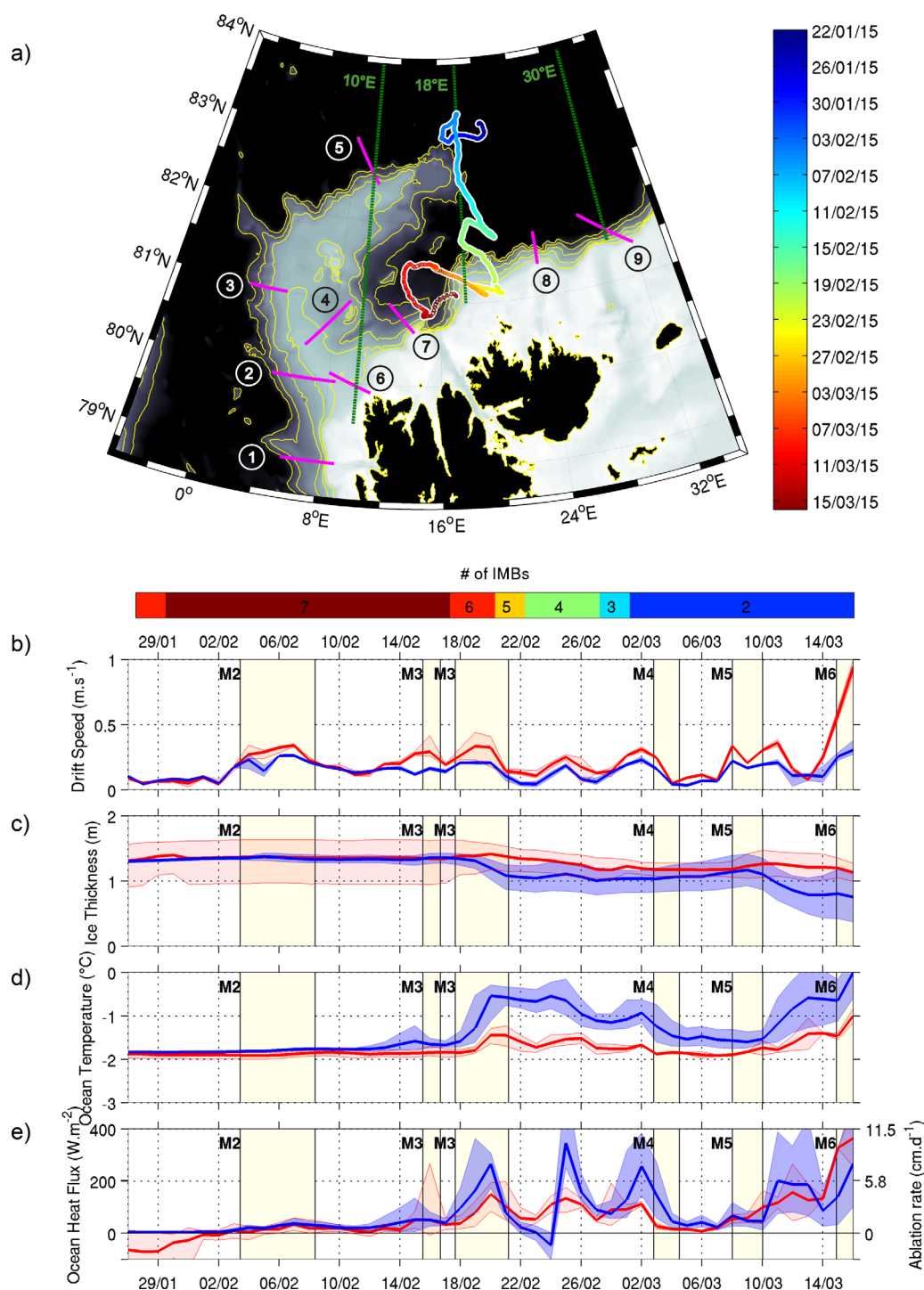
Figure 3. (a) IAOOS platform drift trajectory. The color of the drift is the date. Background is bathymetry (m). The yellow isolines are bathymetry contours (500, 700, 1000, 1500, and 2000m). The purple segments 1–9 indicate the sections through which the volume transports are calculated (Table 1). The green lines show the sections at 10,18 and 30°E used in Figures 7b–7e: Comparisons of model outputs (in blue) (mean and range in a 20 km radius around the IAOOS platform) to observations from SIMBAs (in red, mean and range of the SIMBA observations): (b) Drift speed (ms^{-1}). (c) Ice thickness (m). (d) Ocean temperature (°C). (e) Ocean heat flux density (Wm^{-2}) and corresponding ablation rate (m d^{-1}) (Ocean heat flux being considered as latent heat flux). M1–M6 indicate the storms described in *Hudson and Cohen* [submitted]. The top colorbar indicates the number of SIMBAs available along the time series.

extracted and collocated model outputs in a 20 km radius around the IAOOS platform location along the drift (corresponding to 4–5 grid cells) to examine model reproduction of the variables listed above. Since model variable outputs are daily means, observations were daily averaged (Figure 3).

The ice-tethered ocean profilers measured temperature, salinity, and dissolved oxygen in the upper 500 m twice a day. The data gathered by the three profilers were averaged to produce a composite section of upper ocean temperature and salinity with the same vertical resolution as the model outputs and a daily resolution (the model time resolution) along the platform drift (Figures 4a and 4c). As in *Koenig et al.* [2016], we used the International Thermodynamic Equations Seawater framework [*McDougall et al.*, 2012] with conservative temperature CT (°C) and absolute salinity SA (g kg^{-1}). We then produced model-derived sections of conservative temperature and absolute salinity, over the upper 500 m collocated with the profiler observations (Figures 4b and 4d).

3. Comparison Between Mercator Ocean and N-ICE2015 IAOOS Observations

3.1. Comparison With SIMBA Data

Six main storms (M1, . . ., M6) were identified with wind speeds in excess of 8 ms^{-1} [*Hudson and Cohen*, 2015] (L. Cohen et al., Meteorological conditions in a thinner Arctic sea ice regime from winter through spring during the Norwegian young sea ICE expedition (N-ICE2015), submitted to *Journal of Geophysical Research Oceans*, 2017) (Figure 3). Daily means of modeled ice drift speed (in blue) are of the same order of magnitude as daily means of SIMBA drift velocities (in red) with most values between 10 and 20 cms^{-1} and larger values up to 40 cms^{-1} during storms and over the continental slope off Svalbard (after March 10) (Figure 3b). However, model ice drift during storms is smaller than observations by about 10 cms^{-1}. Model ice thickness agrees with the mean of the observed values (1.30–1.40m) until 17 February, and then decreases faster than in the observations (Figure 3c). Ice thickness is more spatially homogeneous in the model (range less than 10 cm) than in the observations (range about 70 cm) until 18 February; the range in ice thickness then increases in the model after the strong melt centered on 20 February indicative of an inhomogeneous melt. Indeed, model ocean surface temperatures (precisely 50 cm below sea surface) span quite a large range about 1°C between 18 and 26 February, whereas they are homogeneous until 10 February. Model surface ocean temperatures are always warmer than those observed, the difference being larger after 10 February with model temperature peaks at −0.5°C, instead of −1°C in the in situ data (Figure 3d). Model surface ocean temperatures are above the model freezing temperature (−1.88°C) after 2 February. Consequently modeled ocean fluxes, positive after 2 February, are large and often larger than ocean-to-ice fluxes estimated from the SIMBA (Figure 3e). Peaks in modeled ocean fluxes are consistent with those observed in magnitude and time. Modeled ocean fluxes correspond to basal melt rates that can reach up to 12 cm per day (Figure 3e).

3.2. Ocean Water Masses: Comparison With Profiler Data

Temperature and salinity in the model outputs, collocated in space and time with the winter IAOOS profiler data, show patterns similar to those observed (Figure 4). The water masses encountered in the model outputs are in good agreement with the in situ observations in winter 2015 (Figure 4): at depth, Modified Atlantic Water (MAW, T < 2°C and the density $27.7 < \sigma < 27.95$) and Atlantic water (AW, T > 2°C and $27.7 < \sigma < 27.95$), and near the surface, Polar Surface Water (density $\sigma < 27.7$) (definition of water masses from *Rudels et al.* [2000] used by *Koenig et al.* [2016] and *Meyer et al.* [2017].

MAW is found in the Nansen Basin with a core depth at 300 m, that is 50 m deeper than in the observations. AW is observed over the continental slope of Svalbard (from 13 February to 21 February) in the boundary current with characteristics similar to those in the observations (core depth around 250 m, T~3°C, S~35.25 g.kg^{-1}), and along the northern and eastern tip of the Yermak Plateau (from 27 January to 3 February and from 6 February to 11 February, core depth around 300 m, T~2.5°C, S~35.2 g.kg^{-1}). The offshore limit of the AW originating from the Svalbard Branch in the model outputs is in good agreement with the in situ data (Figure 1 at 82.3°N and 19°E).

The warm water (AW) from the Yermak Branch observed on 8–9 February in the IAOOS data (Figure 1 at 83°N and 19°E and Figure 4a) is seen twice in the model, first between 27 January and 3 February and a second time between 7 and 13 February (Figure 4b). In the model outputs, the flow is coming from the Yermak
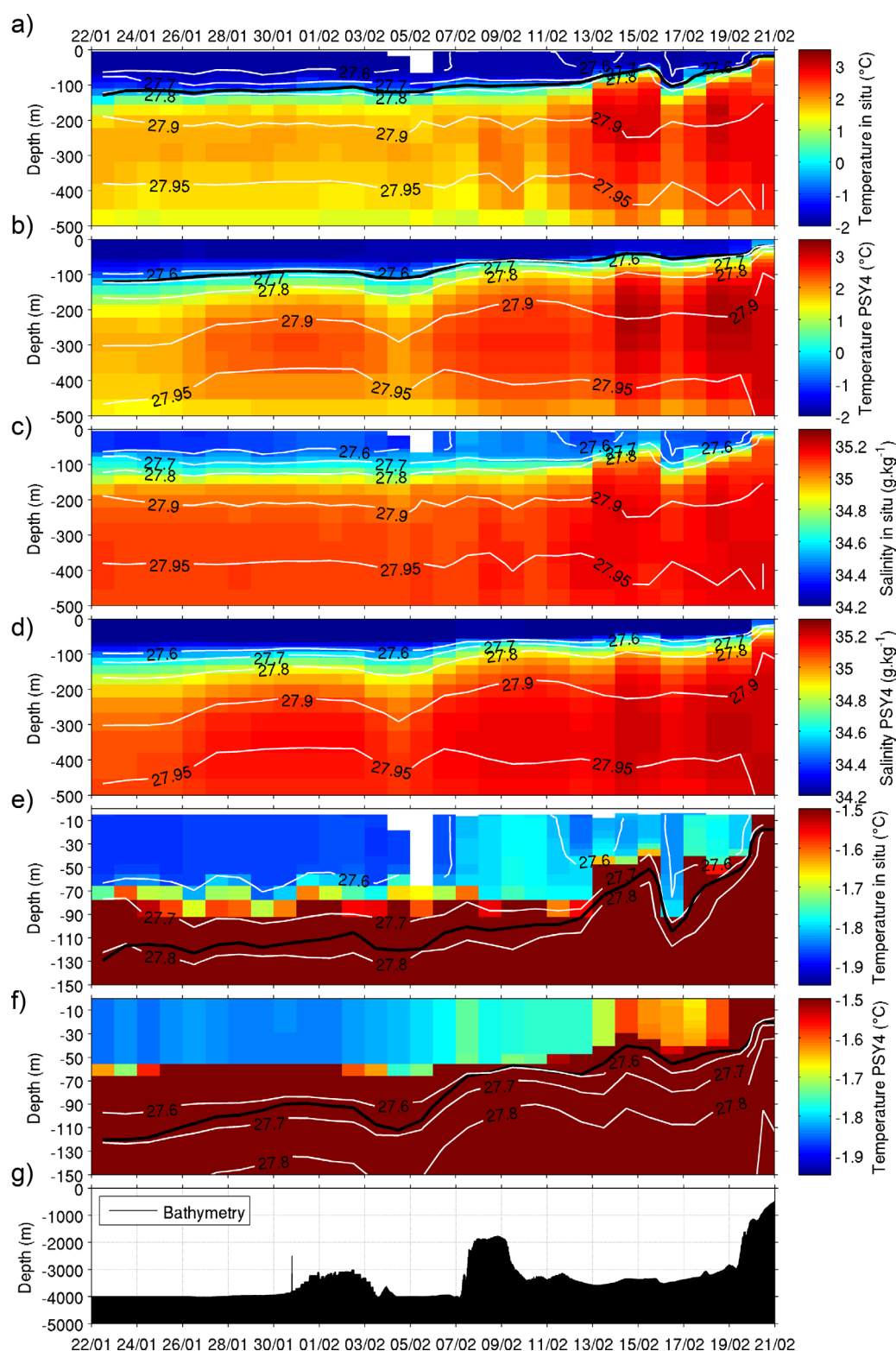
Figure 4. Hydrography from data and model. Data along the drift are daily averaged. Daily model outputs are collocated with IAOOS platform data. (a) Conservative Temperature from IAOOS ocean profilers in the upper 500 m (in °C). (b) Conservative Temperature from model (called PSY4 in the figure) (in °C). (c) Absolute Salinity from IAOOS ocean profilers over the upper 500 m (g.kg^{-1}). (d) Absolute Salinity from model (g.kg^{-1}). (e) Close-up of Conservative Temperature over the upper 100 m from IAOOS profilers (°C). (f) Close-up of Conservative Temperature over the upper 100 m from model (°C). In all plots, white lines are isopycnals. The black line in Figures 4a, 4b, 4e, and 4f is the 0°C isotherm. (g) Bathymetry along the drift in meter.

Branch in the form of pulsing eddies and is highly variable (section 4.2). Model temperatures in the core of the warm layer at 82.5°N and 18°E vary between 2 and 2.8°C while the observed temperature on 8 February at that location are ~2.1°C within the model range.

The modeled mixed layer temperature is in good agreement with the in situ data with above freezing temperature over the Yermak Plateau (−1.75°C) and values of −1.55°C over the Svalbard continental slope (Figures 4e and 4f). The modeled mixed layer salinity is smaller by about 0.25 g.kg^{-1}, its variations from one location to another are comparable to the in situ salinity. Fresher mixed layer in the model outputs results in a stronger pycnocline in the model than in the observations (Figure 4). The modeled depths of the 0°C isotherm and of the pycnocline, at ~105 m depth at the beginning and up to ~20 m depth at the end, are comparable with the in situ data.

In summary, in spite of a mixed layer that is too fresh, the hydrography of the model is in good agreement with the winter IAOOS data. Model outputs were also compared (not shown) with the CTD data from a free-
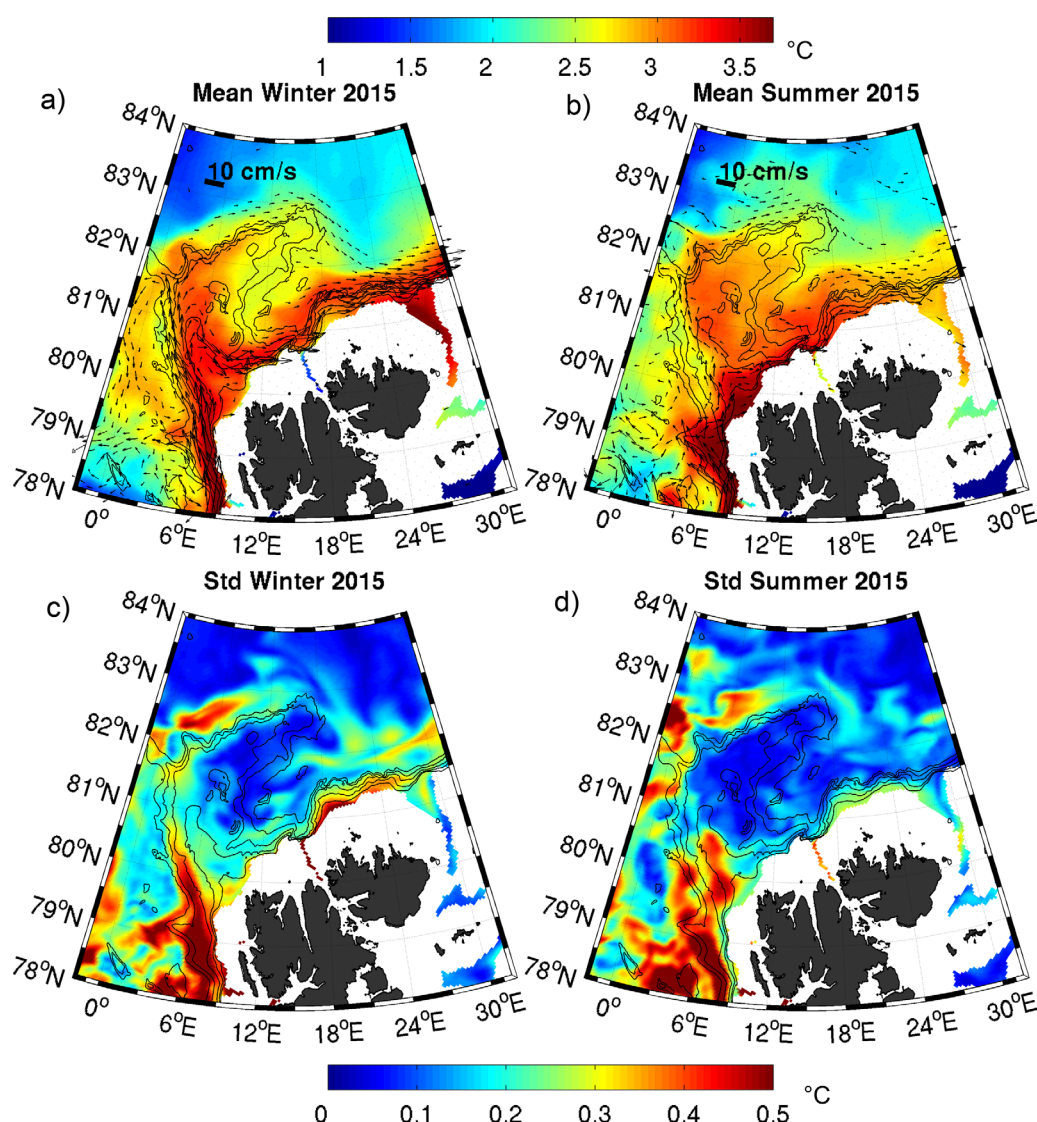

Figure 5. (top) Mean circulation (arrows in cms^{-1}) and Conservative Temperature (°C) from the model outputs for the layer centered at 266 m (50 m thick) over (a) January–February–March 2015 and (b) July–August–September 2015. The corresponding colorbar (in °C) is at the top of the figure. (bottom) Standard deviation of the Conservative Temperature (°C) for the layer centered at 266 m (50 m thick) over (c) January–February–March 2015 and (d) July–August–September 2015. White areas are shallower than 266 m. The corresponding colorbar (in °C) is at the bottom of the figure.

falling microstructure profiler (0–300 m) deployed during N-ICE2015 until 18 June 2015 [*Meyer et al.*, 2017]. Again the hydrography of the model was in remarkable agreement with the data, the only differences being a too fresh mixed layer in general (by 0.25 g.kg^{-1}) and a too shallow mixed layer over the Yermak Plateau (by 20 m). As the model ice-edge follows satellite observations, we believe that the model performances can be trusted in summer and autumn although there are no hydrographic data available in the region in summer or autumn 2015 for a precise comparison.

4. Warm Water Layer: Inferences From Model Outputs

4.1. Warm Water Pathways, Volume Transports, and Heat Contents in 2015

Warm water paths are examined using winter (January–March) and summer (July–September) mean temperature maps with mean velocity vectors in the core of the AW layer (266 m) (Figures 5a and 5b) and using time series of volume transport and heat content in the AW layer (T>2°C) through nine sections across the AW pathways (purple lines in Figure 3a and Table 1). Heat content of the warm water layer (T>2°C) in each transect was computed as in *Lique and Steele* [2013]: $\int_{z0}^{zl} \rho_0 C_p (T(t,x,y,z) - T_{ref}) dz$ with ρ_0 the density of ocean water, C_p the ocean specific heat (4000 J.kg^{-1}.K^{-1}), and T_{ref} a reference temperature (here -1.8°C).

In 2015, AW pathways differ in winter and summer (Figures 5a and 5b). In winter, the large AW volume transport of the West Spitsbergen Current (WSC) (section 1, $\sim$ 4 Sv) proceeds to the north-east through three branches: the Svalbard Branch (section 6, 0.5 Sv) along the northern continental slope of Svalbard, the Yermak Branch (section 5, 0.3 Sv) along the western slope of the Yermak Plateau, and the Yermak Pass Branch (section 4, 1.8 Sv) over a pass in the Yermak Plateau at 80.8°N. This passage was observed by floats [*Gascard et al.*, 1995] and recalled by *Rudels et al.* [2000]. The flow in that pass follows the 600–700 m isobaths and joins the Svalbard continental slope around 10°E (Figure 5a). The Yermak Branch, well defined on the western slope of the Yermak Plateau, is weaker on the northern and eastern slope of the Yermak Plateau. The Yermak Branch can be followed all along the slope of the Yermak Plateau, and joins the Svalbard continental slope at around 20°E.

In summer 2015, the AW transport in the WSC is smaller (section 1, $\sim$2 Sv) and there is no transport through the Yermak Pass (section 4) (Figures 5b and Table 1). The connection from the AW inflow at 78°N to the Svalbard Branch follows the northern continental slope of the Svalbard Archipelago above 400–500 m, as described in *Sirevaag et al.*, [2011] and *Muench et al.*, [1992]. A large part of the Yermak Branch bifurcates to the north-northwest at the tip of the Yermak Plateau and the flow joining the Svalbard continental slope is weaker than in winter.

Several bifurcations to the west back into Fram Strait are observed along the AW path: a first one both in summer and winter at about 79°N [e.g., *Von Appen et al.*, 2016], a second one larger in winter than summer at about 81.5°N [*Hattermann et al*, 2016], and a third one at 82.5°N (12°E) on the northern side of the Yermak Plateau larger in summer than in winter (Figure 5b).

Table 1. Volume Transport Statistics (in Sv) Across Several Sections Over the Yermak Plateau and the Svalbard Continental Slope for the Water Warmer Than 2°C (AW Pathways)[a]

2014 *2015*	79°N *1*	80°N *2*	81°N *3*	YPB *4*	YB *5*	SB *6*	12°E *7*	24°E *8*	30°E *9*
Mean	**2.8**	**1.7**	**0.9**	**1.1**	**0.4**	**0.4**	**1.5**	**1.8**	**2.1**
	2.8	*1.9*	*1.0*	*0.7*	*0.4*	*0.7*	*1.6*	*1.8*	*1.9*
Summer mean	**2.1**	**1.2**	**0.2**	**0.6**	**0.6**	**0.5**	**1.1**	**1.2**	**1.6**
	1.3	*1.1*	*0.8*	*−0.4*	*0.5*	*0.8*	*0.9*	*0.9*	*1.0*
Winter mean	**3.9**	**2.1**	**1.1**	**1.5**	**0.2**	**0.5**	**1.8**	**2.5**	**2.6**
	4.0	*2.8*	*1.7*	*2.1*	*0.4*	*0.4*	*2.3*	*2.9*	*3.1*
Std	**1.4**	**0.9**	**0.7**	**0.7**	**0.3**	**0.5**	**0.6**	**0.8**	**0.88**
	1.8	*1.0*	*0.7*	*1.1*	*0.2*	*0.6*	*0.8*	*1.2*	*1.2*
Summer std	**1.5**	**0.7**	**0.7**	**0.4**	**0.2**	**0.3**	**0.2**	**0.5**	**0.5**
	1.3	*0.6*	*0.3*	*0.3*	*0.1*	*0.3*	*0.4*	*0.4*	*0.5*
Winter Std	**1.2**	**1.0**	**0.4**	**1.0**	**0.1**	**0.7**	**0.7**	**1.0**	**1.0**
	1.5	*0.8*	*0.7*	*0.9*	*0.3*	*0.7*	*0.7*	*0.9*	*0.8*

[a]In bold: statistics for year 2014, In italic: statistics for year 2015. Winter: January–February–March. Summer: July–August–September.
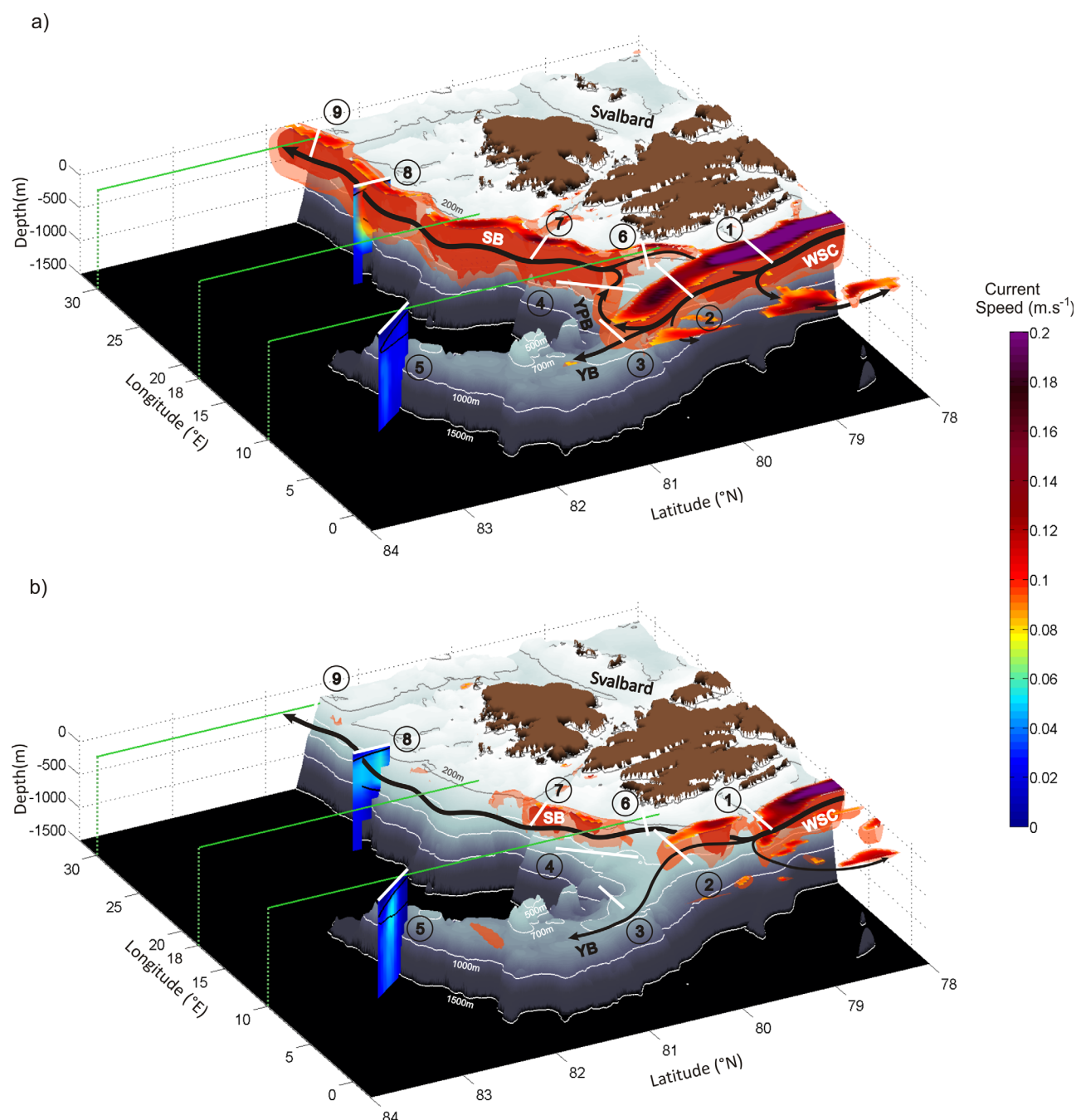
Figure 6. 3-D representation of AW winter and summer current pathways (color bar in ms^{-1}). Two speed cores are plotted: dark red inner core is 0.12 ms^{-1} and pale red outer core 0.08 ms^{-1}. (a) Winter mean (January–February–March) and (b) summer mean (July–August–September). The transects 1–9 (white lines at the surface) correspond to the sections through which the volume transport and heat content are calculated (Table 1 and Figure 7). Cross-track velocity is shown for sections 5 and 8 (the black isoline is the 0°C isotherm). The background is the bathymetry. Transects at 10, 18 and 30°E used in Figure 8 are indicated in green. SB: Svalbard Branch. YB: Yermak Branch. YPB: Yermak Pass Branch. WSC: West Spitsbergen Current.

The large seasonal variations in AW described above for year 2015 are also found in 2014 (Table 1) and are illustrated in a composite 3-D plot (three winters: 2014, 2015, and 2016 and two summers: 2014 and 2015) (Figure 6) with a strong winter circulation featuring an overflow in the Yermak Pass and a weaker summer circulation. In yearly and seasonal means, the transport at 12°E (section 7) is roughly the sum of the transports through the Yermak Pass Branch (section 4) and Svalbard Branch (section 6) while the transport at 24°E (section 8) corresponds to the sum of the transport at 12°E (section 7) and the transport through the Yermak Branch (section 5) (Table 1). Differences between the volume transports at 79°N (section 1) and

80°N (section 2) are due to the recirculation to the west which is larger in winter (1.5 Sv) than in summer (0.5 Sv) (Table 1). Year to year differences are large in the Yermak Pass Branch (section 4) especially in summer with even a reverse flow (-0.4 Sv) in 2015 (Table 1 and Figure 5b).

Heat content of the warm layer decreases away from Fram Strait (Figures 7a–7c). In the WSC, the heat content is larger in summer (33×10^{13} Jm^{-2}) than in winter (18×10^{13} Jm^{-2}). Around the Yermak Plateau, the heat content is larger in the Yermak Pass Branch and the Svalbard Branch (15×10^{13} Jm^{-2} in winter and 20×10^{13} Jm^{-2} in summer) than in the Yermak Branch (less than 8×10^{13} Jm^{-2}) (Figure 7b). Seasonal variations dominate the heat content evolution of the warm layer along the Svalbard continental slope (Figures 8a, 8c, and 8e). Lags between two time series of the warm water heat content (defined as the lag of the maximum correlation between the two time series) can be considered as an advection time scale between the two sections. The lag is 38 days between heat content time series at 79°N and 80°N (r = 0.5) (sections 1 and 2) and 50 days between 79°N and 81°N (r = 0.35) (sections 1 and 3) (Figure 7a). Along the Svalbard continental slope, the lag between heat content times series at 24°E and 30°E is 27 days (r = 0.7) (sections 8 and 9) and 38 days (r = 0.7) between 12°E and 24°E (sections 7 and 8) (Figure 7c). These time scales correspond to reasonable mean advection velocities in the warm layer of about 5 cms^{-1}. Correlations between heat content time series at 79°N and the sections across the northern continental slope of Svalbard are not significant (Figures 7a and 7c). Two years and three months of model outputs are not a long-enough time series to examine in detail the links between variations in heat content in the WSC and in the Svalbard Branch at 30°E.

4.2. Subseasonal Activity in the Warm Layer

>Summer and winter standard deviations in temperature at 266 m (the approximate depth of the core of the warm water layer, Figures 5c and 5d) provide some spatial and temporal information about the subseasonal activity in the warm water layer. Large temperature standard deviation (std) (std > 0.5°C, Figures 5c and 5d) corresponding to large intraseasonal variations in volume transport are found along the WSC and on the western side of the Yermak Plateau in agreement with the literature [e.g., *Hattermann et al.*, 2016; *Kawasaki and Hasumi*, 2016]. Intraseasonal variations are also found on the northern and eastern side of the Yermak Plateau (std∼0.2°C), and along the Svalbard Branch (std∼0.35°C in winter and 0.25°C in summer). Volume transports of the warm (>2°C) water layer in most sections exhibit large variations at intraseasonal time scales with large standard deviations in winter and summer (Table 1).

The time-latitude plots of velocity and temperature at 10, 18, and 30°E document the high-frequency variations superimposed over the seasonal variations (Figure 8). At the northern tip of the Yermak Plateau, the Yermak Branch flows in pulses in eddy-like structures observed around 82.5°N in the two sections 10°E and 18°E both in temperature and velocity (Figures 8a–8d). The 18°E section is close to the IAOOS platform drift and shows large temperature variations at 82.5°N in February 2015. The modeled temperature range over a month at that location encompasses the IAOOS observations. Although the comparison of values collocated in time and space may suggest that the model is slightly too warm (Figures 4a and 4b), mesoscale pulses of the Yermak Branch provide temperature variations explaining differences between model and observations.

At 30°E, in the Svalbard Branch, pulsing temperature and velocity structures extend as north as 82.5°N (April 2014, Figure 8). They correspond to warm eddies offshore the continental slope in agreement with *Våge et al.* [2016]. These eddies do not undergo large seasonality and have a short-time scale along these sections (less than a month, Figure 8). A model with a higher spatial resolution is needed to precisely study the eddy field north of Svalbard.

5. Evolution of Ice Edge Location and Near Surface Ocean Temperature From January 2014 to April 2016

Although ice concentration data is not assimilated, the model reproduces satellite-derived ice edge variations (Figure 9). To first order, ice edge displacement are governed by wind direction [e.g., *Thorndike and Colony*, 1982; *Kwok et al.*, 2013]. The strong winter winds (January–March) (mean of 7.2 ms^{-1}) turning counterclockwise around 8°E push the ice edge away from the northern Svalbard coast while the southward
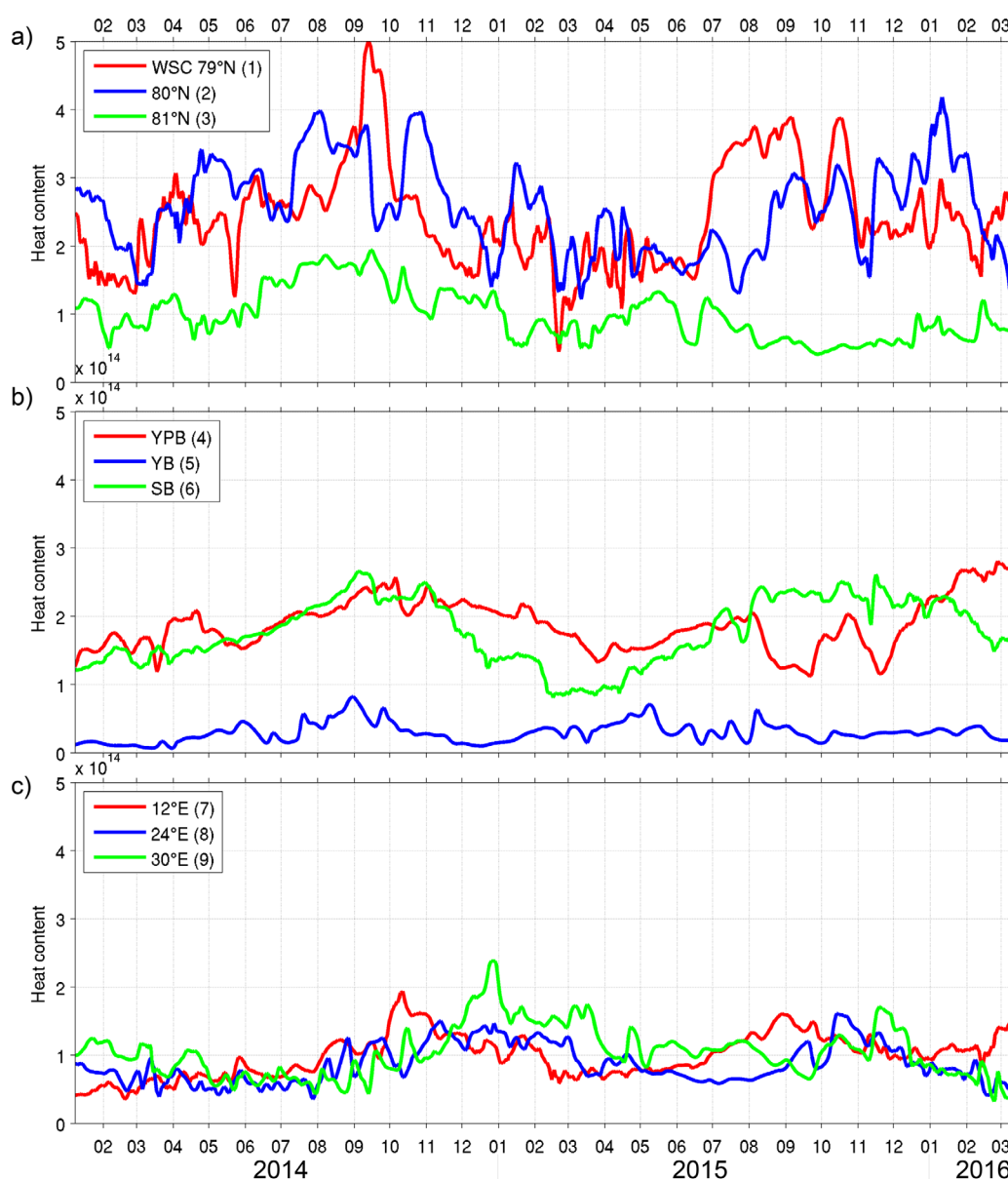
Figure 7. Time series of heat content (in Jm^{-2}) in the different sections numbered in Figures 1 and 6. (a) Sections 1, 2, 3 at 79°N, 80°N and 81°N. (b) Sections 4, 5, 6 across the Yermak Pass Branch (YPB), the Yermak Branch (YB), and the Svalbard Branch (SB). (c) Sections 7, 8, 9 across the continental slope at 12°E, 24°E and 30°E.

spring winds (southeastward in 2014 and southwestward in 2015) (mean speed of 5.2 ms^{-1}) bring the ice edge back close to Svalbard. Warm near surface ocean temperatures (T> 0°C) extend to the northeast in autumn and winter (Figure 9) when the strong positive wind stress curl above continental slope could induce an intense upwelling (order of 30 cmd^{-1}) (Figure 10). This upwelling occurs as the warm water volume transport over Svalbard Branch reaches its seasonal maximum as documented in section 4 (e.g., Table 1 and Figure 8). The large temperature values along the slope in winter can be caused by the upwelling of warm water.

Beyond these broad seasonal variations, year-to-year variations are observed with a much reduced ice cover in summer 2015 (24%) compared to summer 2014 (45%) and in particular less open water in winter 2015 during N-ICE2015 (mean ice cover over the plotted area: 76%) than in winter 2014 and 2016 (mean ice cover over the plotted area: 68% and 57%, respectively) (Figure 9). We focus on the differences that led to very contrasted synoptic situations in winters 2015 and 2016.
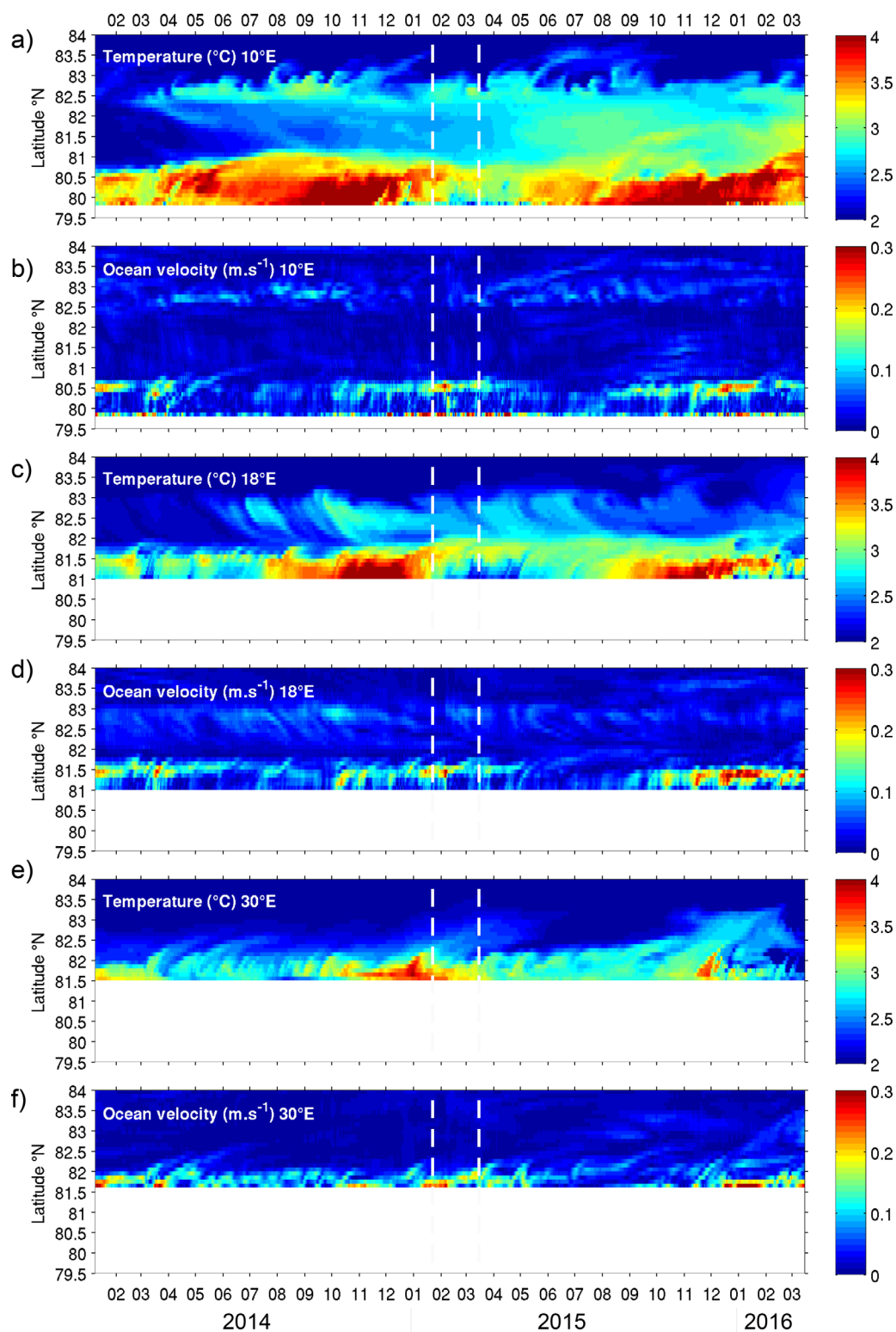
Figure 8. Evolution of (b, d, and f) ocean velocity (ms^{-1}) and (a c and e) temperature (°C) for the layer centered at 266 m (40 m thick) from January 2014 to April 2016 along meridional sections at (a and b) 10°E, (c and d) 18°E, and (e and f) 30°E. The vertical-dashed lines mark the beginning and the end of the in situ measurement from floe 1 of N-ICE 2015 campaign.
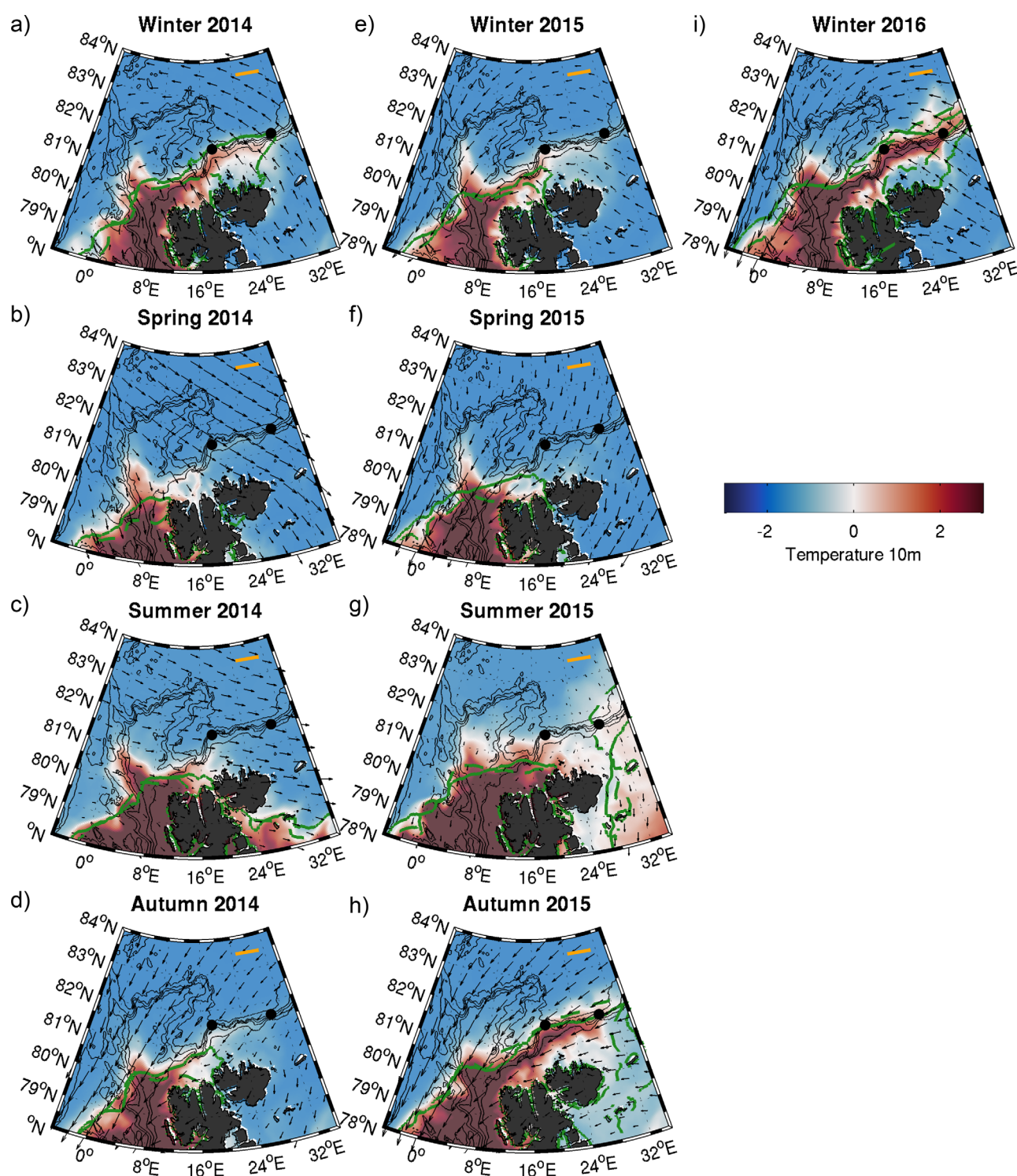
Figure 9. Wind speed at 10 m (arrows) averaged every 3 months from January 2014 to March 2016. (top right) The orange scale corresponds to 5 ms^{-1}.The green solid line (green-dashed line) is the 15% mean sea ice cover contour from AMSR-2 (model outputs) over the period and is taken as the location of the ice edge. The background color is the mean modeled ocean temperature at 10 m over the designated period. The thin black lines are the bathymetry contours. The black dots on the continental slope at 18°E and 30°E indicate the location of the shown profiles in Figure 12.

In summer 2014, westerlies (mean speed about 2 ms^{-1}) are pushing the ice toward Svalbard whereas in 2015 summer winds are extremely weak (Figures 9c and 9g). Furthermore summer 2015 air temperatures on the continental slope east of Svalbard are 0.5°C warmer than the year before (1°C instead of 0.5°C, not shown).
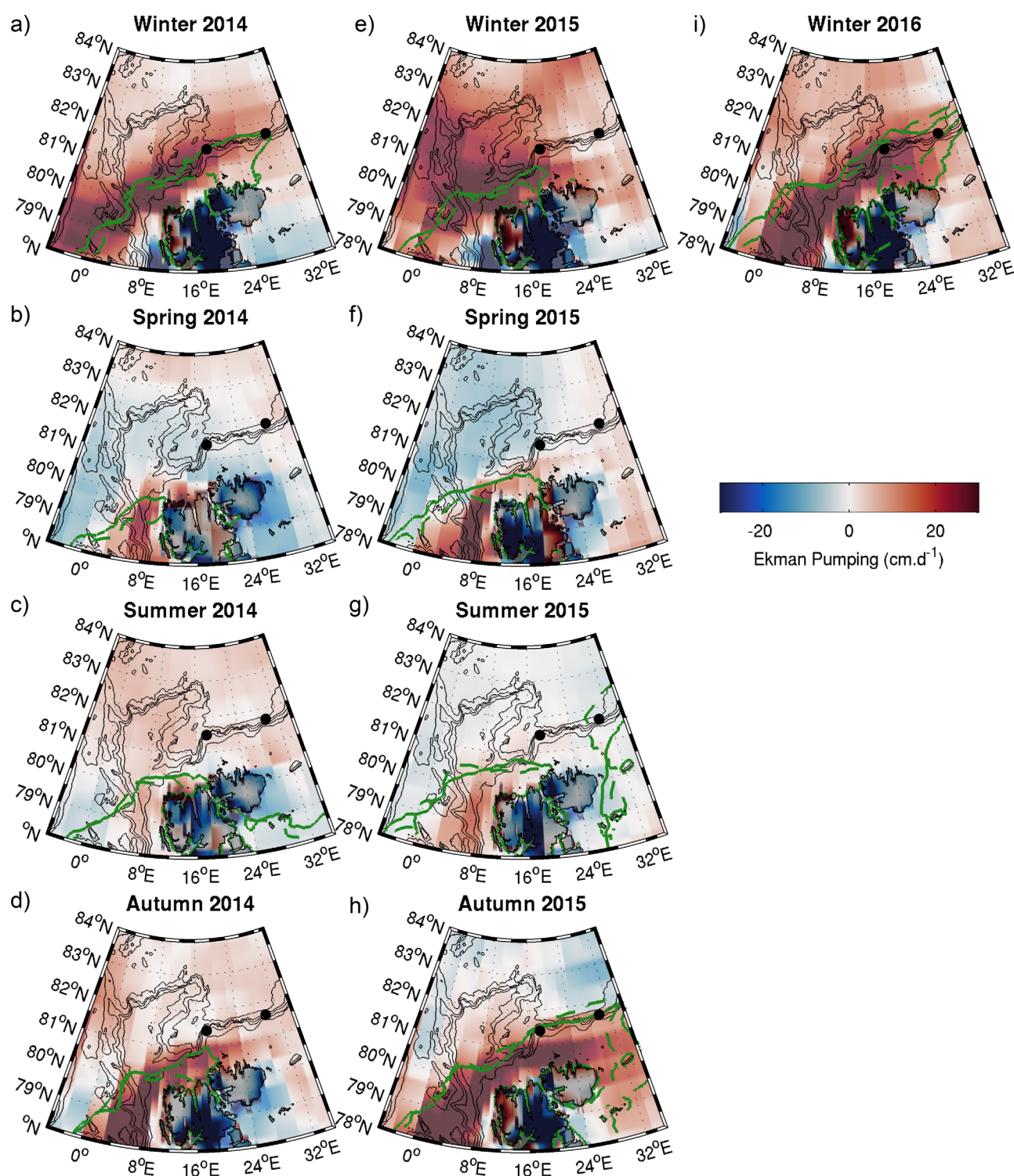
Figure 10. Ekman pumping (cm.d^{-1}) averaged every 3 months from January 2014 to March 2016. The Ekman pumping is computed from the wind stress from ECMWF (http://apps.ecmwf.int/datasets/data/interim-full-daily). The green solid line (green-dashed line) is the 15% mean sea ice cover contour from AMSR-2 (model outputs) over the period and is taken as the location of the ice edge. The thin black lines are the bathymetry contours. The black dots on the continental slope at 18°E and 30°E indicate the location of the shown profiles in Figure 12.

Time-latitude plots of wind intensity, air temperature, Ekman pumping, ocean velocity, and temperatures at 10 m provide some insight into the year-to-year variations at 18°E around the location of the N-ICE2015 drift in winter and at 30°E around the A-Twain mooring site [*Våge et al.*, 2016] (Figure 11). Wind speed and air
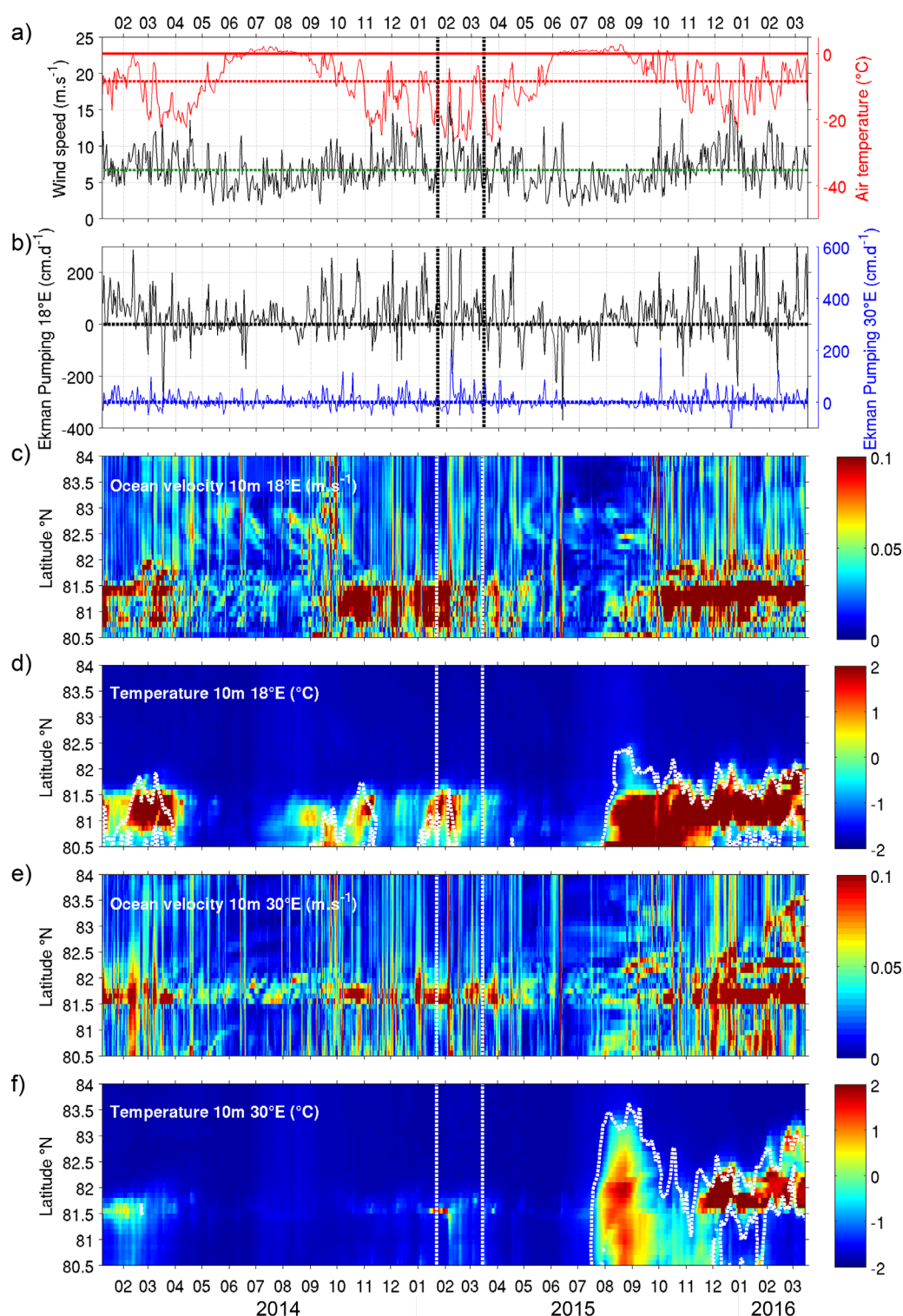
Figure 11. Evolution of model variables along 18°E and 30°E from January 2014 to April 2016. (a) Integrated wind speed over the latitudes at 18°E (ms^{-1}) (right axis). The dashed green line is the mean wind speed. (left axis) Integrated air temperature over the latitudes at 18°E. The dashed red line is the mean air temperature. (b) Ekman pumping (cmd^{-1}) averaged over the latitudes at 18°E (left axis) and 30°E (right axis). The black (blue) dashed line is the mean Ekman pumping at 18°E (30°E). (c) and (e) Ocean velocity of the layer centered at 10 m (ms^{-1}) at 18°E (30°E). (d) and (f) Model temperature of the layer centered at 10 m (°C) at 180°E (30°E). The dashed black line is the ice edge (the 15% isoline) from the model. The vertical dashed lines mark the beginning and the end of the in situ measurement from Floe 1 during N-ICE 2015 campaign.
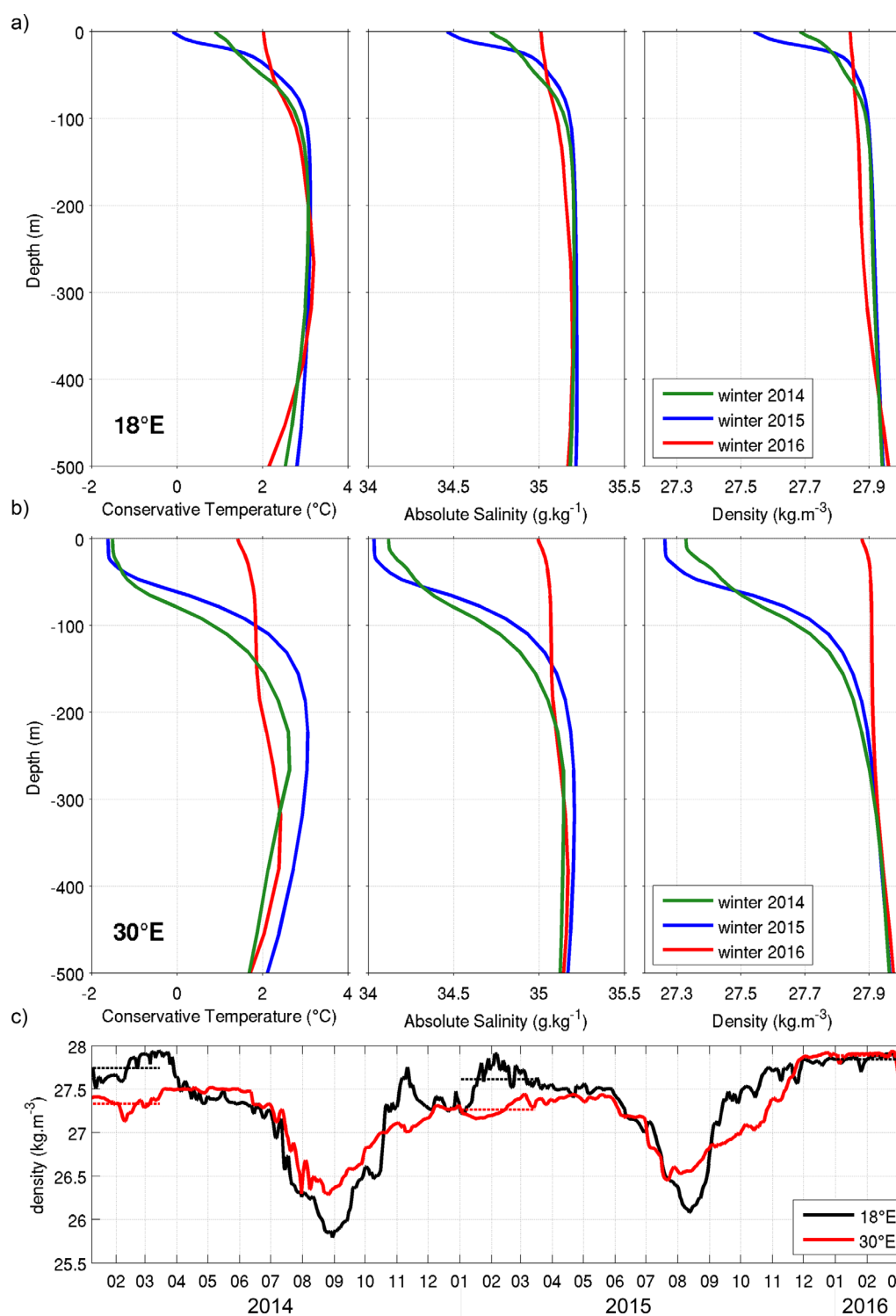
Figure 12. (a) Mean profiles of conservative temperature (°C), absolute salinity (g.kg^{-1}) and potential density (kg.m^{-3}) at 18°E, 81.4°N. (b) at 30°E, 81.85°N (black dots in Figures 9 and 10). The green profiles are averaged over winter 2014, the blue ones over winter 2015, and the red ones over winter 2016. (c) Time series of potential density (kg.m^{-3}) at 10m at 18°E, 81.4°N (in black), and at 30°E, 81.85°N (in red).

temperature time series are shown for only one site (18°E) as they do not differ much from one site to the other (Figure 11a). In contrast, Ekman pumping time series are strikingly different with values at 18°E almost one order of magnitude larger than those at 30°E (Figure 11b). At both locations, variations in ice cover are particularly striking and well correlated with ocean temperatures at 10 m with the open water in autumn

2015 and winter 2016 associated with temperatures larger than 2°C (Figures 11d and 11f). Ocean velocities at 10 m are dominated by the seasonal cycle with large values in autumn and winter and high-frequency variations reflecting wind forcing even under the ice (ice cover > 15%) (Figures 11a, 11c, and 11e). The temperature and velocity time series in the AW layer do not show any significant year-to-year variation that could be directly related to the surface year-to-year variations (Figures 8c–8f, and temperature at 10 m in Figure 11).

Mean winter vertical profiles of ocean temperature, salinity and density at 18°E and 30°E over the continental slope differ from one winter to the other, with winter 2016 profiles (in red) being much less stratified, the difference being particularly striking at 30°E (Figures 12a and 12b). The time series of surface density show values larger than 27.55 kgm^{-3} each winter at 18°E (in black), whereas at 30°E winter 2016 stands out with values in excess of 27.8 kgm^{-3}, 0.5 kgm^{-3} above the winter 2014 or 2015 values (in red) (Figure 12c).

In winter 2014 and 2015, the slope at 30°E was covered with sea ice and near surface ocean water was much colder and fresher than in winter 2016 (Figures 9–12). In winter 2016, the slope at 30°E was ice-free and the very high ocean surface density values, the homogeneous vertical profiles over the water column and the rather small Ekman pumping suggest deep winter convective mixing in agreement with *Ivanov et al.* [2016]. The winter 2016 situation followed a rather warm and ice-free summer and autumn (Figures 9, 11a and 11f), favoring subsequent winter convective mixing [*Ivanov et al.*, 2016]. In turn, the convection-induced upward heat flux maintained the area free of ice in winter 2016.

The slope at 18°E is at least partially ice-free during the three winters under consideration. Each winter wind-stress curl induced upwelling is large and probably plays an important role in upwelling warm water from the deep [*Falk-Petersen et al.*, 2015]. The rather homogeneous vertical profiles over the water column in winter 2016 suggest however a contribution of convective mixing following the warm ice free summer and autumn as at the 30°E location.

6. Conclusions

Mercator ocean global operational system has been evaluated in the region of the Atlantic Water (AW) inflow, using historical data sets (e.g., the Fram Strait monitoring data) and contemporaneous data (satellite ice cover and IAOOS data collected during N-ICE2015 in winter). The model provides a realistic Atlantic Water inflow in Fram Strait that corresponds in intensity, temperature, and seasonal variations to historical observations in the West Spitsbergen Current (WSC) [*Beszczynska-Moller et al.*, 2012]. The model also remarkably reproduces the hydrographical features observed by the IAOOS profilers in the Atlantic Water north of Svalbard in winter. Although the model is only eddy permitting and not fully eddy resolving in the Arctic, it produces mesoscale features that are consistent with those observed during the winter IAOOS drift. It helps interpretation of the in situ data in terms of warm water paths and eddy activity [*Koenig et al.*, 2016].

Model outputs were used to examine the circulation of Atlantic Water at the entrance to the Arctic Ocean. Apart from recirculation branches to the West back into Fram Strait, the WSC splits into three warm water paths over and around the Yermak Plateau: the Svalbard Branch following the northern continental slope of the Svalbard Archipelago along the 400–500 m isobath [*Muench et al.*, 1992], the Yermak Branch flowing along the western slope of the Yermak Plateau along the 1000 m isobath [*Manley et al.*, 1992], and a third branch going through a narrow 700 m-deep depression in the Yermak Plateau, the Yermak Pass Branch, that was previously observed in deep float trajectories [*Gascard et al.*, 1995].

The volume transports of the three branches (T>2°C) exhibit large seasonal variations in phase with the WSC volume transport that almost doubles in winter compared to summer [*Beszczynska-Moller et al.*, 2012] (Table 1). The Yermak Pass Branch is mostly a winter feature associated with an overflow of the strong winter WSC. During the three winters of the model outputs (2014, 2015, and 2016), more than 70% of the WSC volume transport at 80°N goes through the Yermak Pass in winter, with a particularly large value (75%) in winter 2015 at the time of the IAOOS observations [*Koenig et al.*, 2016]. The Yermak Pass Branch shows up as a warm feature in the AW layer crossed between the 6 and 13 February in both the observations and model outputs (Figure 4). Beyond the dominant seasonal variations, intraseasonal and year-to-year variations in the AW volume transport of the three branches above and around the Yermak Plateau can be almost as large as the mean amplitude (Table 1).

The three branches recombine further east along the Svalbard northern continental slope (Figure 1) and the volume transports in the AW layer along the slope at 12°E, 24°E, and 30°E show again a coherent seasonal cycle in phase with the WSC with large winter values. The heat content in the AW layer (T>2°C) decreases away from Fram Strait as expected and varies seasonally. Lags in the seasonal variations of the heat content time series provide rough estimates of advection time scales that are coherent with mean velocities (5 cms^{-1}) along the western (79 and 80°N) and northern (12, 24, and 30°E) continental slopes of Svalbard considered separately (Figure 7). However, correlations in heat content between 79°N and the sections further east (12, 24 and 30°E) cannot be established in a 2.25 year long-time series.

Although the eddy-permitting model (4–5 km grid) does not fully explicitly resolve the Rossby radius of deformation in this area (6–8 km) [*Zhao et al.*, 2014; *Nurser and Bacon*, 2013], outputs point out to a large mesoscale activity and a flow in form of pulses in the branches over and around the Yermak Plateau, and in the flow along the continental slope (Figure 8 and std values in Table 1). Mesoscale activity in the WSC and on the western side of the Yermak Plateau is in agreement with the literature [e.g., *Hattermann et al.*, 2016; *Kawasaki and Hasumi*, 2016]. Model also shows the detachment of eddies from the boundary current on the slope in agreement with the N-ICE2015 IAOOS observations [*Koenig et al.*, 2016] and observations at 30°E [e.g., *Våge et al.*, 2016].

Compared to 2016, winter 2015 stands out with colder air temperatures (mean −19°C versus −9°C), larger sea ice cover (mean ice cover around the Svalbard 76% versus 57%) and colder ocean temperatures at 10 m on the continental slope to the northeast of Svalbard (Figure 10). A qualitative consideration of the wind, ice extent, and temperature (surface atmosphere and 10 m depth ocean) sequence from January 2014 to April 2016 (Figure 9–12) tends to support the *Ivanov et al.* [2016] concepts that (i) the ice cover (wind forced ice drift) and water temperature in summer and autumn appear to "precondition" the situation for the coming winter and (ii) wind stress curl-induced ocean upwelling and convective mixing are key drivers for supplying ocean heat to the surface and maintaining an ocean ice free area in winter along the continental slope (section 5). The relative importance of Ekman pumping and convective mixing along the Svalbard continental slope in maintaining ice-free conditions in winter 2016 requires further analysis. The balance of ocean-atmosphere heat fluxes, not examined here, needs to be carefully examined as well.

The short-time span of the model outputs analyzed here (2.25 years) precludes any significant statistical analysis in a system with large year-to-year variations and expected long-term trends [*Lind and Ingvaldsen*, 2012; *Onarheim et al.*, 2014; *Ivanov et al*, 2012, 2016]. Such longer time scales trends and variability are the subject of future investigation since 10 years (2007–present) of date from the Mercator Ocean global operational model are now available.

References

Aksenov, Y., V. V. Ivanov, A. J. Nurser, S. Bacon, I. V. Polyakov, A. C. Coward, A. C. Naveira-Garabato, *and* A. Beszczynska-Moeller (2011), The Arctic circumpolar boundary current, *J. Geophys. Res.*, 116, C09017, doi:10.1029/2010JC006637.

Beszczynska-Moller, A., E. Fahrbach, U. Schauer, and E. Hansen (2012), Variability in Atlantic water temperature and transport at the entrance to the Arctic Ocean, 1997–2010, *ICES J. Mar. Sci.*, 69, 852–863.

Cokelet, E. D., N. Tervalon, and J. G. Bellingham (2008), Hydrography of the West Spitsbergen Current, Svalbard Branch: Autumn 2001, *J. Geophys. Res.*, 113, C01006, doi:10.1029/2007JC004150.

Dmitrenko, I. A., B. Rudels, S. A. Kirillov, Y. O. Aksenov, V. S. Lien, V. V. Ivanov, U. Schauer, I. V. Polyakov, A. Coward, and D. G. Barber (2015), Atlantic water flow into the Arctic Ocean through the St. Anna Trough in the northern Kara Sea, *J. Geophys. Res. Oceans*, 120, 5158–5178, doi:10.1002/2015JC010804.

Falk-Petersen, S., V. Pavlov, J. Berge, F. Cottier, K.M. Kovacs, and C. Lydersen (2015), At the rainbow's end: High productivity fueled by winter upwelling along an Arctic shelf, *Polar Biol.*, 38, 5–11, doi:10.1007/s00300-014-1482-1.

Gascard, J.-C., C. Richez, and C. Rouault (1995), New insights on large-scale oceanography in Fram Strait: The West Spitsbergen Current, in *Arctic Oceanography, Marginal Ice Zones and Continental Shelves*, vol. 49, edited by W. O. Smith and J. M. Greibmeier, pp. 131–182, AGU, Washington, D. C.

Granskog, M. A., P. Assmy, S. Gerland, G. Spreen, H. Steen, and L. H. Smedsrud (2016), Arctic research on thin ice: Consequences of Arctic sea ice loss, *Eos*, 97, 22–26, doi:10.1029/2016EO044097.

Hattermann, T., P.E. Isachsen, W-J. von Appen, J. Albretsen, and A. Sundfjord (2016), Eddy-driven recirculation of Atlantic Water in Fram Strait, *Geophys. Res. Lett.*, 43, 3406–3414, doi:10.1002/2016GL068323.

Hernandez, F., et al. (2015). Recent progress in performance evaluations and near real-time assessment of operational ocean products, *J. Oper. Oceanogr.*, 8, suppl 2, s221–s238, doi:10.1080/1755876X.2015.1050282.

Hudson, S. R., and L. Cohen (2015), N-ICE2015 surface meteorology v1, Norwegian Polar Inst., Tromsø, Norway. [Available at https://data.npolar.no/dataset/056a61d1-d089-483a-a256-081de4f3308d.]

Ilıcak, M. et al. (2016), An assessment of the Arctic Ocean in a suite of interannual CORE-II simulations. Part III: Hydrography and fluxes, *Ocean Modell.*, 100, 141–161, doi:10.1016/j.ocemod.2016.02.004.

Ivanov, V., I. Polyakov, I. Dmitrenko, E. Hansen, I. Repina, S. Kirillov, C. Mauritzen, H. Simmons, and L. Timokhov (2009), Seasonal variability in Atlantic Water off Spitzbergen, *Deep Sea Res., Part I*, *56*, 1–14.

Ivanov, V. V., V. A. Alexeev, I. A. Repina, N. V. Koldunov, and A. V. Smirnov (2012), Tracing Atlantic Water signature in the Arctic sea ice cover east of Svalbard, *Adv. Meteorol.*, *2012*, 11, doi:10.1155/2012/201818.

Ivanov, V. V., V. Alexeev, N. Koldunov, I. Repina, A. Sandø, L. Smedsrud, and A. Smirnov (2016), Arctic Ocean heat impact on regional ice decay: A suggested positive feedback, *J. Phys. Oceanogr.*, *46*, 1437–1456, doi:10.1175/JPO-D-15-0144.1

Jackson, K., J. Wilkinson, T. Maksym, D. Meldrum, J. Beckers, C. Haas, and D. Mackenzie (2013), A novel and low-coast sea ice mass balance buoy, *J. Atmos. Oceanic Technol.*, *30*, 2676–2688, doi:10.1175/JTECH-D-13-00058.1.

Kawasaki, T., and H. Hasumi (2016), The inflow of Atlantic water at the Fram Strait and its interannual variability, *J. Geophys. Res. Oceans*, *121*, 502–519, doi:10.1002/2015JC011375.

Koenig, Z., C. Provost, N. Villacieros-Robineau, N. Sennéchael, and A. Meyer (2016), Winter ocean-ice interactions under thin sea ice observed by IAOOS platforms during N-ICE 2015: Salty surface mixed layer and active basal melt, *J. Geophys. Res. Oceans*, *121*, 7898–7916, doi:10.1002/2016JC012195.

Kwok, R., G. Spreen, and S. Pang (2013), Arctic sea ice circulation and drift speed: Decadal trends and ocean currents, *J. Geophys. Res. Oceans*, *118*, 2408–2425, doi:10.1002/jgrc.20191.

Lellouche, J. M., et al. (2013), Evaluation of real time and future global monitoring and forecasting systems at Mercator Ocean, *Ocean Sci. Discuss.*, *9*, 1123–1185.

Lien, V. S., S. S. Hjøllo, M. D. Skogen, E. Svendsen, H. Wehde, L. Bertino, F. Counillon, M. Chevallier, and G. Garric (2016), An assessment of the added value from data assimilation on modeled Nordic Seas hydrography and ocean transports. *Ocean Modell.*, *99*, 43–59, doi: 10.1016/j.ocemod.2015.12.010.

Lind, S., and R. B. Ingvaldsen (2012). Variability and impacts of Atlantic Water entering the Barents Sea from the north, *Deep Sea Res., Part I*, *62*, 70–88.

Lique, C., and M. Steele (2012), Where can we find a seasonal cycle of the Atlantic water temperature within the Arctic Basin?, *J. Geophys. Res.*, *117*, C03026, doi:10.1029/2011JC007612.

Lique, C., and M. Steele (2013), Seasonal to decadal variability of Arctic Ocean heat content: A model-based analysis and implications for autonomous observing systems, *J. Geophys. Res. Oceans*, *118*, 1673–1695, doi:10.1002/jgrc.20127.

Madec, G. (2008), NEMO ocean engine. Note du pôle de modélisation, vol. 27, Inst. Pierre-Simon Laplace (IPSL), France.

Manley, T. O., R. H. Bourke, and K. L. Hunkins (1992), Near-surface circulation over the Yermak Plateau in northern Fram Strait, *J. Mar. Syst.*, *3*(1), 107–125.

McDougall, T. J., D. R. Jackett, F. J. Millero, R. Pawlowicz, and P. M. Barker (2012), A global algorithm for estimating Absolute Salinity, *Ocean Sci.*, *8*, 1123–1134.

Meyer A., et al., (2017), Winter to summer oceanographic observations in the Arctic Ocean north of Svalbard, *J.Geophys. Res.*, doi: 10.1002/2016JC012391.

Muench, R. D., M. G. McPhee, C. A. Paulson, and J. H. Morison (1992), Winter oceanographic conditions in the Fram Strait-Yermak Plateau region. *J. Geophys. Res.*, *97*(C3), 3469–3483.

Nurser, A. J. G., and S. Bacon (2013), Eddy length scales and the Rossby radius in the Arctic Ocean, *Ocean Sci. Discuss.*, *10*(5), 1807–1831.

Onarheim, I. H., L. H. Smedsrud, R. B. Ingvaldsen, and F. Nilsen (2014), Loss of sea ice during winter north of Svalbard, *Tellus Ser. A*, *66*, 1600-0870, doi:10.3402/tellusa.v66.23933.

Pham, D. T., J. Verron, and M. C. Roubaud (1998), A singular evaluative extended Kalman filter for data assimilation in oceanography, *J. Mar. Syst.*, *16*, 323–340.

Provost, C., et al. (2015), Ice-atmosphere-Arctic ocean observing system, 2011–2019, *Mercator Ocean Quart. Newsl., Mercator Ocean*, *51*, 13–15. [Available at http://www.mercator-ocean.fr/eng/actualitesagenda/newsletter/newsletter-Newsletter-51-Special-Issue-with-ICE-ARC.]

Rudels, B. (2012), Arctic Ocean circulation and variability–advection and external forcing encounter constraints and local processes. *Ocean Sci.*, *8*(2), 261–286, doi:10.5194/os-8-261-2012.

Rudels, B., R. Meyer, E. Fahrbach, V. V. Ivanov, S. Østerhus, D. Quadfasel, U. Schauer, V. Tverberg, and R. A. Woodgate (2000), Water mass distribution in Fram Strait and over the Yermak Plateau in summer 1997. *Ann. Geophys. 18*(6), 687–705.

Ryan, A. G., et al. (2015). GODAE Ocean View Class 4 forecast verification framework: Global ocean inter-comparison, *J. Oper. Oceanogr.*, *8*(S1), s98–s111.

Sirevaag, A., S. D. L. Rosa, I. Fer, M. Nicolaus, M. Tjernström, and M. G. McPhee (2011), Mixing, heat fluxes and heat content evolution of the Arctic Ocean mixed layer, *Ocean Sci.*, *7*(3), 335–349, doi:10.5194/os-7-335-2011.

Thorndike, A. S., and R. Colony (1982), Sea ice motion in response to geostrophic winds, *J. Geophys. Res.*, *87*(C8), 5845–5852.

Våge, K., R. S. Pickart, V. Pavlov, P. Lin, D. J. Torres, R. Ingvaldsen, A. Sundfjord, and A. Proshutinsky (2016), The Atlantic Water boundary current in the Nansen Basin: Transport and mechanisms of lateral exchange, *J. Geophys. Res. Oceans*, *121*, 6946–6960, doi:10.1002/2016JC011715.

Von Appen, W.-J., U. Schauer, T. Hattermann, and A. Beszczynska-Möller (2016), Seasonal cycle of mesoscale instability of the West Spitsbergen Current, *J. Phys. Oceanogr.*, *46*, 1231–1254, doi:10.1175/JPO-D-15-0184.1.

Zhao, M., M.-L. Timmermans, S. Cole, R. Krishfield, A. Proshutinsky, and J. Toole (2014), Characterizing the eddy field in the Arctic Ocean halocline, *J. Geophys. Res. Oceans*, *119*, 8800–8817, doi:10.1002/2014JC010488.